energies

MDPI

Article

EL-to-IV: Deep Learning-Based Prediction of Photovoltaic Current-Voltage Curves from Electroluminescence Imaging

Mahmoud Dhimish [1,*], Gisele Alves dos Reis Benatto [1], Romênia G. Vieira [2] and Peter Behrensdorff Poulsen [1]

[1] Department of Electrical and Photonics Engineering, Technical University of Denmark, 4000 Roskilde, Denmark; garb@dtu.dk (G.A.d.R.B.); ppou@dtu.dk (P.B.P.)
[2] Department of Engineering and Technology, Semi-Arid Federal University—UFERSA, Mossoro 59625-900, RN, Brazil; romenia.vieira@ufersa.edu.br
* Correspondence: mahdh@dtu.dk

Abstract

Accurate current–voltage (IV) characterization is essential for assessing photovoltaic (PV) module performance, yet conventional IV tracing requires physical contact and controlled conditions, limiting large-scale deployment. Electroluminescence (EL) imaging, while highly effective for detecting localized defects, remains largely qualitative and indirect in estimating actual PV module power loss. This study introduces a deep learning framework that directly predicts complete IV curves from EL images, transforming EL inspection into a quantitative, non-contact diagnostic tool. In this work, we propose a convolutional neural network (CNN) that learns the nonlinear mapping between paired EL images captured at 20% and 80% of the short-circuit current and the corresponding IV response. A total of 438 PV modules were used for model development, with performance evaluated on unseen data. The trained CNN reconstructs IV curves with high fidelity, achieving a validation accuracy of approximately 95% and low parameter deviations (<2% for key metrics such as maximum power point and fill factor). The model maintains consistent accuracy even when a single EL image is provided, supporting flexible field operation. Inference is rapid, requiring less than 0.5 s per PV module inspection, enabling real-time analysis.

Keywords: electroluminescence imaging; IV curve reconstruction; convolutional neural network; photovoltaic module diagnostics; deep learning regression

1. Introduction

Photovoltaic (PV) systems are increasingly deployed at scale as a cornerstone of the global energy transition, making reliable, rapid, and non-invasive performance assessment essential throughout their operational lifetime. The current–voltage (IV) curve remains the most comprehensive electrical descriptor of PV module behavior [1–3], short-circuit current, open-circuit voltage, maximum power point, and loss mechanisms arising from degradation [4,5] or manufacturing defects [6]. Accurate IV characterization underpins performance benchmarking, fault diagnosis, degradation analysis, and asset valuation [7–10]. However, conventional IV measurements require physical electrical access, controlled operating conditions, and often system downtime, which limits their practicality for large-scale or in-field inspection campaigns.

Electroluminescence (EL) imaging has emerged as a powerful optical diagnostic technique for identifying spatially resolved defects in PV modules [11,12], including microcracks, shunts, series resistance effects, and material inhomogeneities [13,14]. By visualizing

Academic Editor: Carlo Renno

Received: 18 January 2026
Revised: 30 January 2026
Accepted: 1 February 2026
Published: 8 February 2026

recombination-related radiative emission under forward electrical bias [15], EL imaging provides detailed insight into the physical condition of individual cells and interconnections within a module. Figure 1 illustrates a typical laboratory-based EL inspection setup, comprising a controlled power supply, EL camera, and data acquisition system, alongside a representative EL image acquired from a full PV module. As shown in Figure 1, spatial non-uniformities in EL intensity reveal defect signatures at the cell level that are otherwise invisible under standard visual inspection. As a result of these capabilities, EL imaging is now widely adopted in laboratory testing, manufacturing quality assurance, and increasingly in field inspections, including drone-based night-time surveys [16].

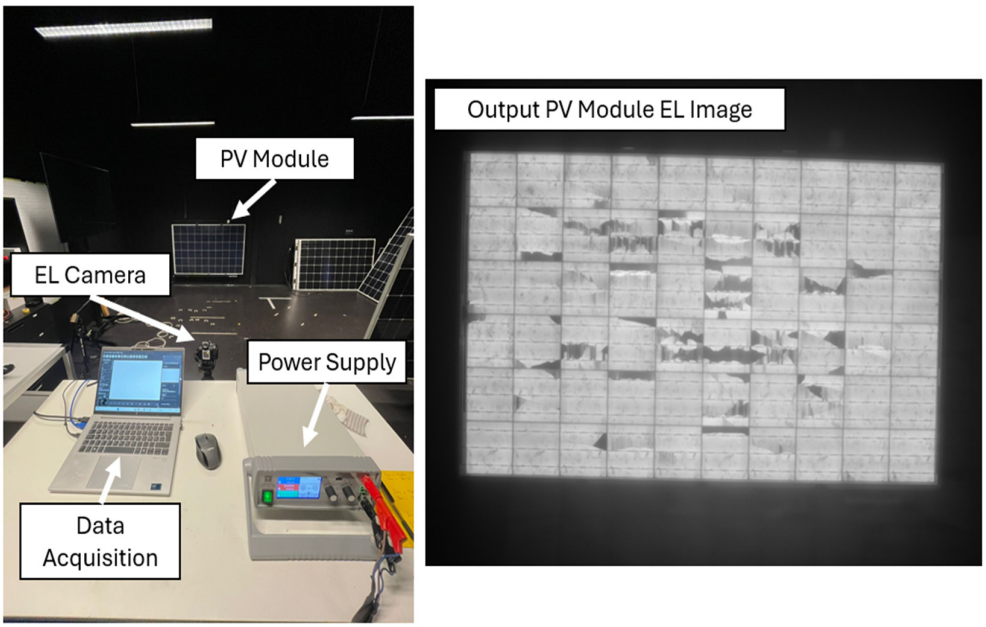

Figure 1. Experimental EL imaging setup and representative output. (**Left**) Laboratory EL inspection arrangement showing the PV module under forward bias, EL camera, power supply, and data acquisition system. (**Right**) Example EL image of a full PV module acquired under controlled conditions, highlighting spatial variations in radiative emission associated with cell-level defects and non-uniform electrical behavior.

Recent advances in machine learning and computer vision have partially bridged the gap between optical inspection and automated PV diagnostics by exploiting EL images for defect detection, degradation classification, and power-loss assessment. Convolutional neural networks (CNNs) have demonstrated strong capability in identifying crack severity, shunting behavior, and cell-level anomalies directly from EL data. As summarized in Table 1, existing CNN-based approaches span lightweight architectures [17], attention-enhanced models [18], large-scale deployment frameworks [19], hybrid ensemble learning [20], and GAN-augmented pipelines [21]. Despite these advances, the vast majority of studies remain focused on intermediate diagnostic outputs, such as defect labels, health indicators, or statistical correlations with power loss. Crucially, none of these methods attempts to reconstruct the full electrical response of the PV module. As a result, the current–voltage (IV) curve, arguably the most information-rich and comprehensive electrical descriptor of PV performance, remains outside the direct scope of image-based inference from EL imagery.

Table 1. Summary of representative CNN-based EL imaging studies for PV diagnostics.

Reference	Methodology	Key Results
[17]	Lightweight CNN for PV cell defect classification from EL images using EfficientNet-B0 with contrast enhancement (CLAHE), graph channel attention, and focal loss.	High defect classification performance on PVEL-AD dataset (accuracy ≈ 97.8%, F1 ≈ 97.6%) with low computational cost.
[18]	Cascade CNN architecture with Squeeze-and-Excitation (SE) blocks, spatial attention, and prediction fusion for multi-class PV cell defect classification from EL images.	Achieved 96% classification accuracy across 12 defect categories, significantly outperforming standard CNNs and single-stage attention models.
[19]	CNN-based automated cell-level defect classification applied to large-scale nocturnal EL imaging of 5.6 million PV cells across 85,000 modules, enabling statistical defect and degradation analysis.	Demonstrated reliable large-scale defect classification and showed strong empirical correlation between defect prevalence and module-level power loss and degradation trends.
[20]	Hybrid CNN–ensemble learning (CNN-EML) framework combining CNN feature extraction with SVM, KNN, and Random Forest classifiers using a weighted voting strategy for multi-class EL defect classification.	Achieved 95% classification accuracy across nine common solar cell defect types, outperforming standalone CNN and individual ML classifiers.
[21]	GAN-augmented CNN framework, integrating DCGAN with VGG16-based perceptual loss to generate synthetic EL images and improve multi-class PV defect classification under severe data imbalance.	Improved defect classification accuracy from 84% to 90%, with enhanced representation of rare and complex defect classes through high-quality synthetic data.

From a system and asset-management perspective, the persistent separation between imaging diagnostics and electrical characterization represents a critical limitation in current PV inspection practice [22–25]. As highlighted in Table 1, existing EL-based approaches rely either on categorical defect identification or on indirect correlations with measured electrical performance. The ability to infer a complete IV curve directly from imaging data would fundamentally change how PV modules are assessed, enabling non-contact, image-only electrical evaluation without interrupting operation or requiring additional instrumentation. Such a capability would allow EL imaging to evolve from a primarily qualitative diagnostic tool into a quantitative surrogate for electrical testing, offering particular value for large-scale PV plants, inaccessible installations, and rapid screening of deployed assets.

In this context, the present work addresses a set of fundamental questions that have not yet been widely explored in the EL diagnostics literature:

1. Can the complex and highly nonlinear relationship between spatial EL emission patterns and the global electrical behavior of a PV module be learned directly from data?
2. Is it possible to reconstruct the full IV curve, rather than isolated parameters or scalar performance indicators, using EL images alone, without imposing explicit physical models or intermediate electrical measurements?
3. To what extent can EL imagery be treated as a holistic representation of the module's electrical state, rather than merely a map of localized defects?

Building on these questions, this work makes several key contributions. First, it presents the first end-to-end deep learning framework capable of directly reconstructing the full IV curve of a photovoltaic module from EL images, without relying on explicit physical models, equivalent-circuit formulations, or intermediate defect classification. Second, the proposed approach introduces a high-dimensional regression strategy that learns the nonlinear mapping between spatial EL emission patterns and the global electrical response of the PV module, enabling prediction of the complete IV curve rather than isolated electrical parameters. Third, the study demonstrates that accurate IV curve reconstruction can be achieved using a single EL image acquired at either low or high current injection levels, substantially reducing data acquisition requirements and improving suitability for field and drone-based inspections. Finally, the framework is validated on a large set of unseen PV modules, achieving low prediction errors for key electrical parameters with sub-second inference times, while a dedicated failure-case analysis provides insight into the sensitivity of the method to EL image quality and pre-processing.

The remainder of this article is organized as follows. Section 2 describes the dataset acquisition process, image pre-processing steps, and the deep learning architecture developed for EL-to-IV prediction. Section 3 presents the experimental results, including representative case studies, statistical evaluation across the full test set, and an analysis of single-condition EL imaging. Section 4 discusses the implications of the findings, highlighting practical applications, limitations, and potential directions for future research. Finally, Section 5 concludes the paper by summarizing the main contributions and emphasizing the significance of direct IV curve reconstruction from EL imagery for advancing photovoltaic diagnostics.

2. Research Methods and Materials

To address the challenge of reconstructing photovoltaic IV curves from EL imagery, this section details the methodology adopted in the present study, illustrated in Figure 2. It begins with a description of the dataset used, including the acquisition of dual-bias EL images and corresponding IV measurements. The subsequent pre-processing steps are outlined, covering image refinement, normalization, and tensor formation. The architecture of the proposed CNN is then presented, highlighting its design for spatial feature extraction and regression mapping. Finally, the section explains the training strategy, loss function formulation, and evaluation protocol used to ensure robust model performance across diverse PV module conditions.

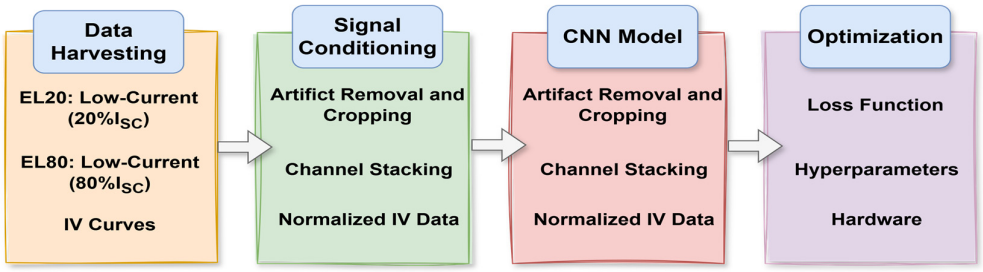

Figure 2. Methodological flowchart.

2.1. Dataset Acquisition and Pre-Processing

The dataset used in this study is publicly available from the Photovoltaic Systems Evaluation Laboratory at Sandia National Laboratories via the Open Energy Information platform (see https://data.openei.org/submissions/8378 accessed on 28 January 2026). It contains 613 PV modules; each measured under two EL biasing conditions, 20% of the short-circuit current (EL20) and 80% of the short-circuit current (EL80), together with the corresponding measured IV curve taken under standard test conditions (irradiance 1000 W/m^2 and temperature 25 °C). These two bias levels were specifically selected to highlight different defect visibility regimes: EL20 enhances the contrast of micro-cracks, shunts and resistive bottlenecks, while EL80 reveals bulk cell degradation, metallization issues and hotspot-related nonuniformities.

An example of the paired EL images and the associated normalized IV curve is shown in Figure 3; further examples from four different PV modules within the dataset are presented in Appendix A. As shown, spatial luminance variations in the EL images directly influence the electrical response of the module, key operating parameters such as current at short circuit (Isc), and voltage at open circuit (Voc) and the maximum power point ($Pmpp = Vmpp \times Impp$) emerge from the underlying physical defects observable in the EL domain. These two EL images were therefore stacked and jointly used as the model input (Section 3.2), providing a complementary and physically grounded representation of PV module health for predicting the full IV curve.

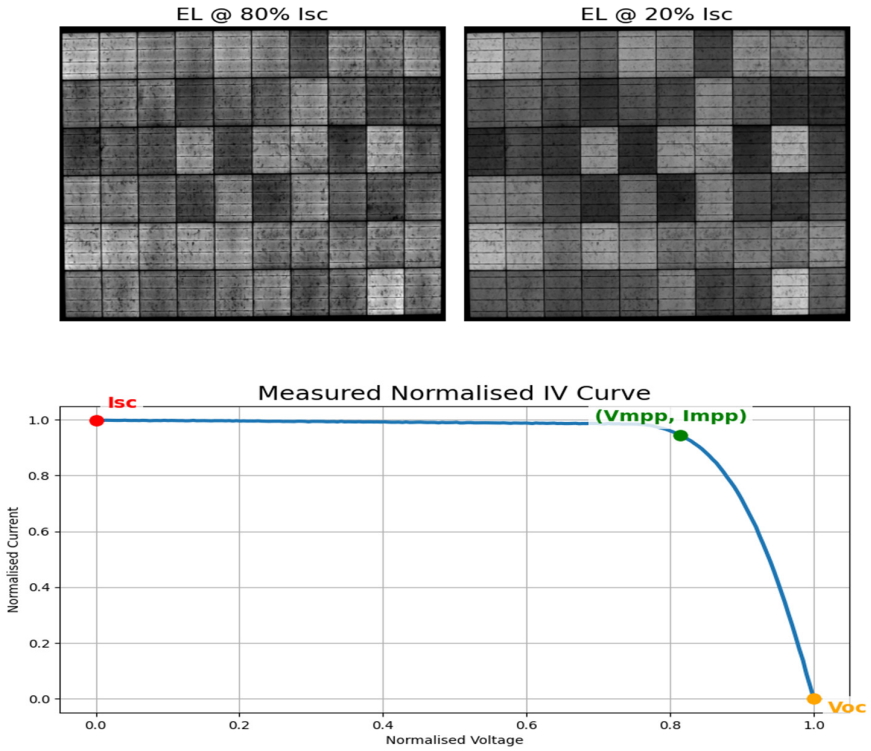

Figure 3. Example of paired EL images and the corresponding measured IV curve.

Raw EL images were originally in high resolution; these images were cropped (see Figure 4) and resized to a fixed spatial resolution of 512 × 512 pixels. Each image was converted to grayscale and normalized to the [0, 1] range by dividing by 255.0. The two bias images for each module were then stacked to form a 512 × 512 × 2 tensor input for the CNN model. The IV curve measurements were provided as tabulated voltage–current pairs. To create a uniform regression target, we performed the following normalization:

1. Voltage was normalized by its maximum value at open-circuit voltage (V/Voc) such that the domain spans 0 to 1. The same process was also applied to the current values and was normalized by its short-circuit current (I/Isc).
2. We then interpolated the normalized IV data onto a fixed grid of 200 equally spaced voltage points using 1D linear interpolation. The resulting vector forms of the regression target were 200-dimensional.

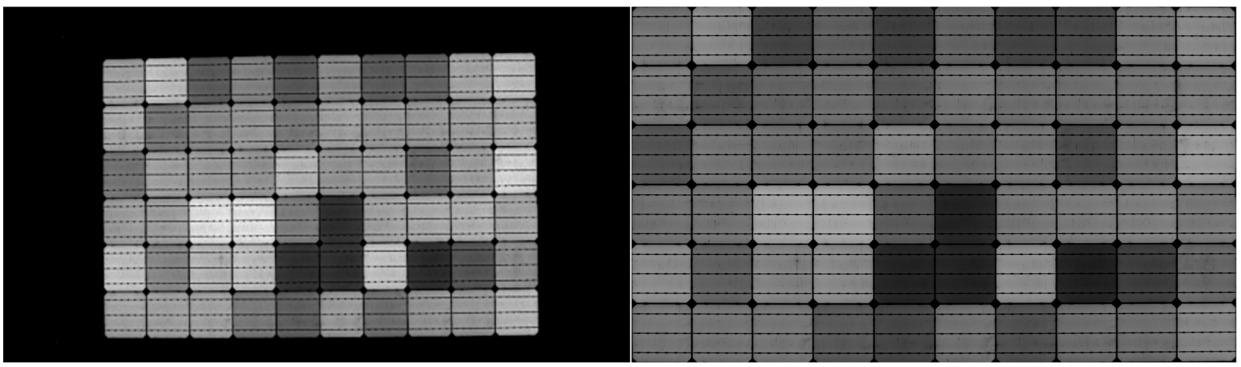

(**a**) (**b**)

Figure 4. Example of EL image pre-processing: (**a**) Original EL image acquired from the dataset, containing full PV module framing and background structures that introduce unwanted noise; (**b**) Cropped EL image used in this study, where background regions have been removed to reduce back-illumination artefacts while retaining the original module geometry.

The design choices adopted during data pre-processing and target construction were guided by a balance between physical fidelity, model stability, and computational efficiency. The EL image resolution was fixed at 512 × 512 pixels to preserve fine spatial defect features (e.g., micro-cracks, shunts, and local non-uniformities) while maintaining feasible memory usage and training time; preliminary testing with lower resolutions (e.g., 256 × 256) led to a noticeable loss of small-scale defect information, whereas higher resolutions provided no measurable performance gain relative to their increased computational cost. The use of two EL images acquired at complementary current injection levels (20% and 80% of *Isc*) was motivated by their distinct physical sensitivity to different defect mechanisms, enabling the model to capture both resistive and bulk degradation effects without introducing unnecessary input redundancy.

For the electrical target representation, the IV curve was interpolated to 200 uniformly spaced voltage points to provide a sufficiently dense yet numerically stable discretization of the curve, ensuring accurate representation of key regions such as the knee near the maximum power point. Normalization of voltage and current by *Voc* and *Isc*, respectively, was applied to decouple defect-induced electrical behavior from absolute module ratings, while interpolation was performed after normalization to preserve the relative shape and smoothness of the IV curve. Empirically, this representation was found to maintain physically meaningful characteristics of the curve, including monotonicity and knee behavior, while enabling robust and consistent regression across modules with varying electrical ratings.

2.2. Deep Learning Model Architecture: EL-to-IV Prediction Model

The proposed deep-learning framework teaches direct, high-dimensional regression mapping from paired EL images to a complete photovoltaic IV curve. Each sample consists of two 512 × 512 grayscale EL images acquired at 80% and 20% of the module short-circuit current (EL80 and EL20), which reveal complementary defect signatures. After preprocessing, these images are stacked along the channel dimension to form a 512 × 512 × 2 tensor, which serves as the model input: $f = R^{512\times512\times2} \rightarrow R^{200}$. The output of the network is a 200-dimensional vector representing the normalized current values sampled uniformly along the voltage axis between 0 and 1. The ground-truth curve is therefore defined as (1).

$$Y_{true} = [I_{true}(v_1), I_{true}(v_2), \ldots\ldots, I_{true}(v_{200})] \quad (1)$$

where v_i is the normalized voltage at the ith sampling point, and I_{true} is the corresponding measured current obtained from the real measured IV curve.

The feature extractor is based on a compact but expressive CNN architecture, designed to learn spatial signatures associated with micro-cracks, metallization defects, shunts, dark regions, and inhomogeneous degradation. The main layers of the built CNN network are summarized in Table 2. ReLU (Rectified Linear Unit) is used throughout the CNN because network because it accelerates convergence [26,27], avoids the vanishing gradient limitations, and works well for sparse defect-related features of the EL images. After the convolutional blocks, global average pooling collapses the 2D feature maps into a compact vector representing overall module health and degradation patterns.

The pooled feature vector is processed by three fully connected layers (see Table 3) with 512, 256 and 128 units, respectively, each followed by a ReLU activation to enhance nonlinearity while avoiding saturation and vanishing-gradient issues. The final output layer consists of 200 units with linear activation because the task requires predicting continuous, real-valued current values along the IV curve. The network's prediction (Y_{pred}) therefore takes the form (2), where $I_{pred}(v_i)$ denotes the model's estimate of the current at voltage v_i.

$$Y_{pred} = \left[I_{pred}(v_1), I_{pred}(v_2), \ldots\ldots, I_{pred}(v_{200}) \right] \quad (2)$$

Table 2. Summary of convolutional layers used for EL feature extraction.

Layer	Filters	Kernel	Stride	Activation	Purpose
Conv2D_1	32	3×3	1	ReLU	Low-level edge & texture extraction
Conv2D_2	32	3×3	1	ReLU	Down sampling and pattern recognition
Max Pooling	—	2×2	2	—	Down sample by 1/2
Conv2D_3	64	3×3	1	ReLU	Detects cracks/shunts at higher feature depth
Conv2D_4	64	3×3	1	ReLU	Spatial abstraction and complexity increase
Max Pooling	—	2×2	2	—	Down sample by 1/2
Conv2D_5	128	3×3	1	ReLU	Learning global degradation morphology
Global Average Pooling	—	—	—	—	Converts spatial feature maps to 1D vector

Table 3. Dense layers used for IV curve regression.

Layer	Units	Activation
Dense_1	512	ReLU
Dense_1	256	ReLU
Dense_1	128	ReLU
Output	200	Linear

To train the model, we use a composite loss function (defined as (3)) consisting of two terms: a point-wise reconstruction loss (L_{MSE}), implemented as the mean squared error (MSE) between the true and predicted current values across all 200 voltage samples, and a smoothness regularization term ($\lambda\ L_{Smooth}$).

$$L = L_{MSE} + \lambda\ L_{Smooth} \quad (3)$$

The weighting parameter λ was set to 0.2 to balance point-wise reconstruction accuracy with smoothness enforcement in the predicted IV curves. Preliminary experimentation with different values of λ indicated that smaller values reduced the effectiveness of the smoothness constraint, occasionally resulting in non-physical local oscillations, particularly near the knee region of the IV curve. Conversely, larger values over-regularized the output and degraded point-wise accuracy by excessively smoothing the curve. The value of $\lambda = 0.2$ was therefore selected as a stable compromise that preserves physically meaningful smoothness while maintaining accurate reconstruction of key electrical characteristics.

The mean squared error is defined as (4), which penalizes point-wise discrepancies between the predicted and measured IV curves. However, because physically realistic IV curves must vary smoothly and monotonically with voltage, we introduce a smoothness term based on the first-order discrete derivative using (5). This term discourages local oscillations and ensures that the predicted curve retains the inherent smoothness of real solar-module behavior. Where $I_{pred}(v_{i+1}) - I_{pred}(v_i)$ is the first discrete derivative of the values; 199 is chosen because the derivative exists only between 200 points, so the maximum is 199.

$$L_{MSE} = \frac{1}{200} \sum_{i=1}^{200} \left(I_{true}(v_i) - I_{pred}(v_i) \right)^2 \quad (4)$$

$$L_{Smooth} = \frac{1}{199} \sum_{i=1}^{199} \left(I_{pred}(v_{i+1}) - I_{pred}(v_i) \right)^2 \quad (5)$$

In total, 438 PV modules were available for analysis after filtering the Sandia dataset for samples containing both valid EL imagery and complete reference IV curves. Although the original dataset comprises 613 PV modules EL image sets, only 438 modules contained (i) both EL20 and EL80 bias-level images of sufficient quality and (ii) a complete measured

IV curve suitable for ground-truth generation. This discrepancy arises from missing EL pairs, inconsistent naming, incomplete IV measurements, and cases where the EL images were not usable due to cropping errors or perspective distortion. For model development, 300 PV modules were used for training and validation, while a separate set of 150 modules was held out as an independent test set that was never seen by the model during training. This ensures that the evaluation reflects true generalization rather than memorization of specific modules.

The model was trained using an 80/20 stratified split at the PV-module level (240 modules for training and 60 for validation), ensuring that all EL images and IV curves from a given module appear exclusively in either the training or validation subset. Training was performed on an NVIDIA A100 GPU (Google Colab Pro, https://colab.google/ accessed on 28 January 2026) using the Adam optimizer (learning rate 10^{-4}) and a batch size of 8. We verified that reducing the batch size to 4 produced comparable results, which is relevant when GPU memory is constrained.

In this paper, "accuracy" refers to the point-wise similarity between the predicted and measured IV curves, evaluated as one minus the normalized mean-squared error (NMSE) over the 200-point discretized IV vector; hence, an accuracy of 100% would indicate a perfect match between predicted and measured IV shapes. Figure 5 shows the training and validation accuracy curves produced by the EL-to-IV CNN network. The model begins with an IV-prediction accuracy of approximately 63% (training) and 60% (validation), followed by a rapid increase during the first 20 epochs as dominant spatial–electrical relationships from EL20/EL80 inputs are learned. Accuracy continues to improve between epochs 20 and 60 as the network learns more subtle degradation-related features that influence the IV shape. The training accuracy eventually stabilizes near 99%, while validation accuracy converges to approximately 95%, demonstrating strong generalization with no observable overfitting. Stabilization occurs at around epoch 80, after which further training yields negligible improvement, consistent with the applied early stopping, learning-rate reduction on plateau, and model checkpointing.

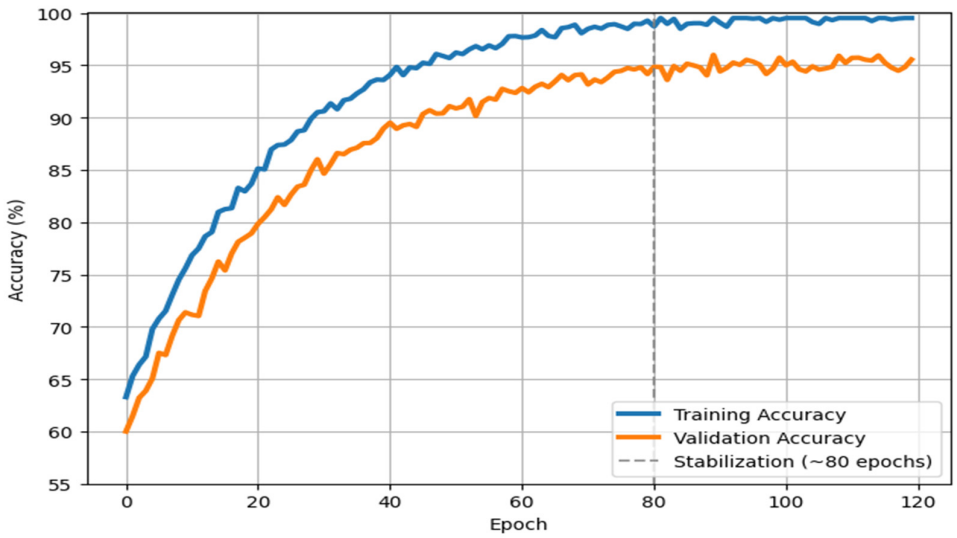

Figure 5. Training and validation accuracy curves for the proposed EL-to-IV prediction model.

In addition, the normalization of the IV curves was introduced to ensure that the proposed EL-to-IV model learns defect-induced electrical behavior independently of the absolute electrical ratings of the PV module. In practice, PV modules may differ in nominal short-circuit current (e.g., 8 A versus 10 A) and open-circuit voltage due to variations in module design, cell technology, or manufacturer specifications. Without normalization,

these rating differences would dominate the regression target and bias the learning process toward absolute current and voltage magnitudes rather than the relative loss mechanisms caused by defects observed in the EL images.

3. Results

3.1. EL-to-IV Prediction Performance on Representative PV Modules

To evaluate the generalization capability of the proposed EL-to-IV prediction model, a dedicated test set of 150 photovoltaic modules, completely unseen during training and validation, was used for performance assessment. This dataset includes a wide range of degradation patterns, luminance distributions, and module operating conditions to ensure that the evaluation reflects realistic field variability. Each test module contains paired EL images acquired at 80% and 20% of the short-circuit current (EL80 and EL20), together with measured IV curves under standard test conditions.

As shown in Figure 6a, PV sample 64 shows a non-uniform luminance distribution in both the EL80 and EL20 images, with several cells exhibiting darker emission patterns that typically correspond to locally reduced current-generating capability. Despite these visually observable defects, the model reconstructs the IV curve with high fidelity. Quantitatively, the predicted *Isc* and *Voc* closely match the measured values, and the power-related parameters (*Pmpp*, *Impp* and *Vmpp*) deviate only marginally (errors <1.4%). The close alignment between the true and predicted curves across the entire voltage range demonstrates that the model has successfully learned the underlying relationship between spatial EL signatures and the global electrical response of the module.

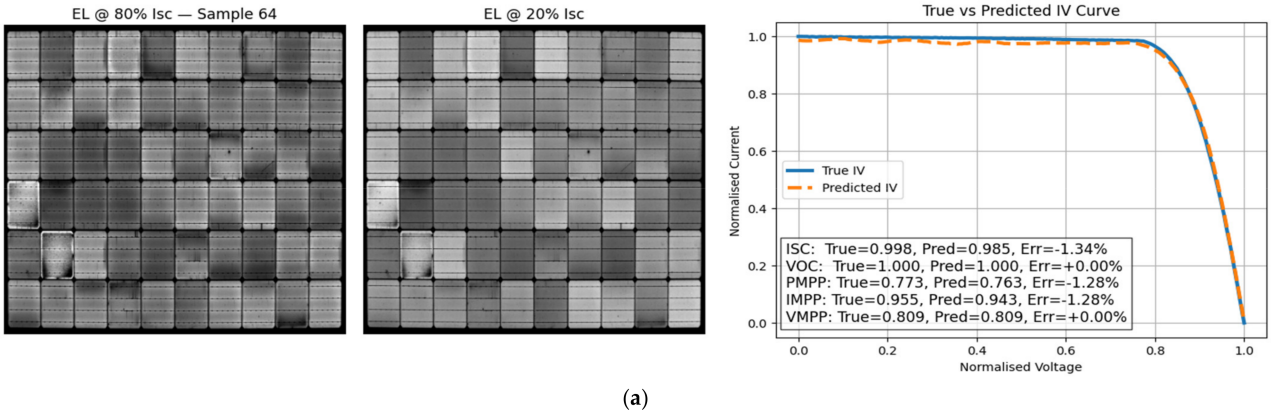

(**a**)

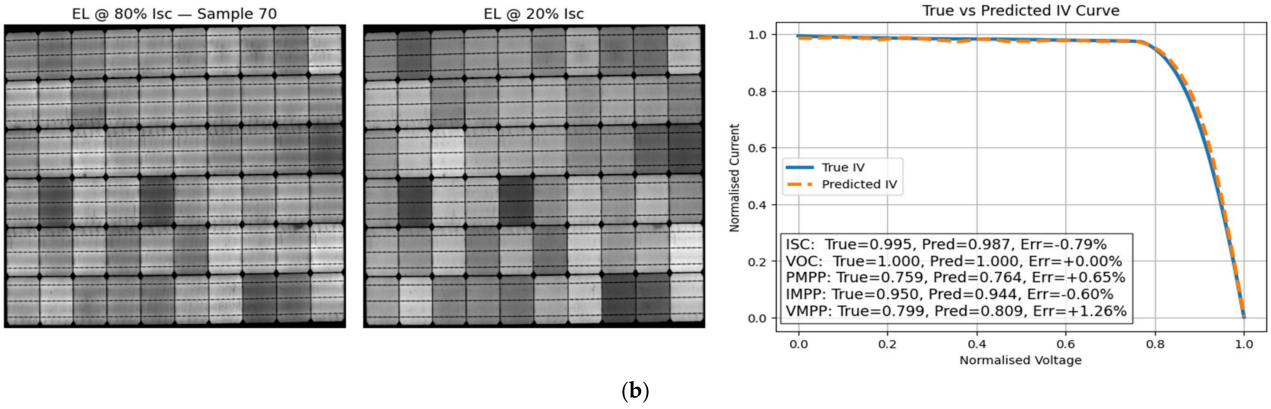

(**b**)

Figure 6. Output EL-to-IV model evaluation: (**a**) Corresponding EL images and IV comparison for Sample 64; (**b**) Corresponding EL images and IV comparison for Sample 70.

PV sample 70 (see Figure 6b) contains several darker and brighter cell clusters, indicating a mixture of series-resistance-related issues and possible shunt-type defects.

Nevertheless, the EL-to-IV model again achieves excellent agreement between predicted and measured IV characteristics. Key performance indicators remain within ±1.26% of their ground-truth values.

In addition to the representative modules shown in Figure 6, further examples from the unseen test set are presented in Figure 7 to demonstrate the robustness of the proposed EL-to-IV model across different PV module types and degradation profiles. These samples were purposely selected to reflect distinct visual characteristics observed in the EL images, including variations in module architecture, EL intensity mismatch, and degradation severity.

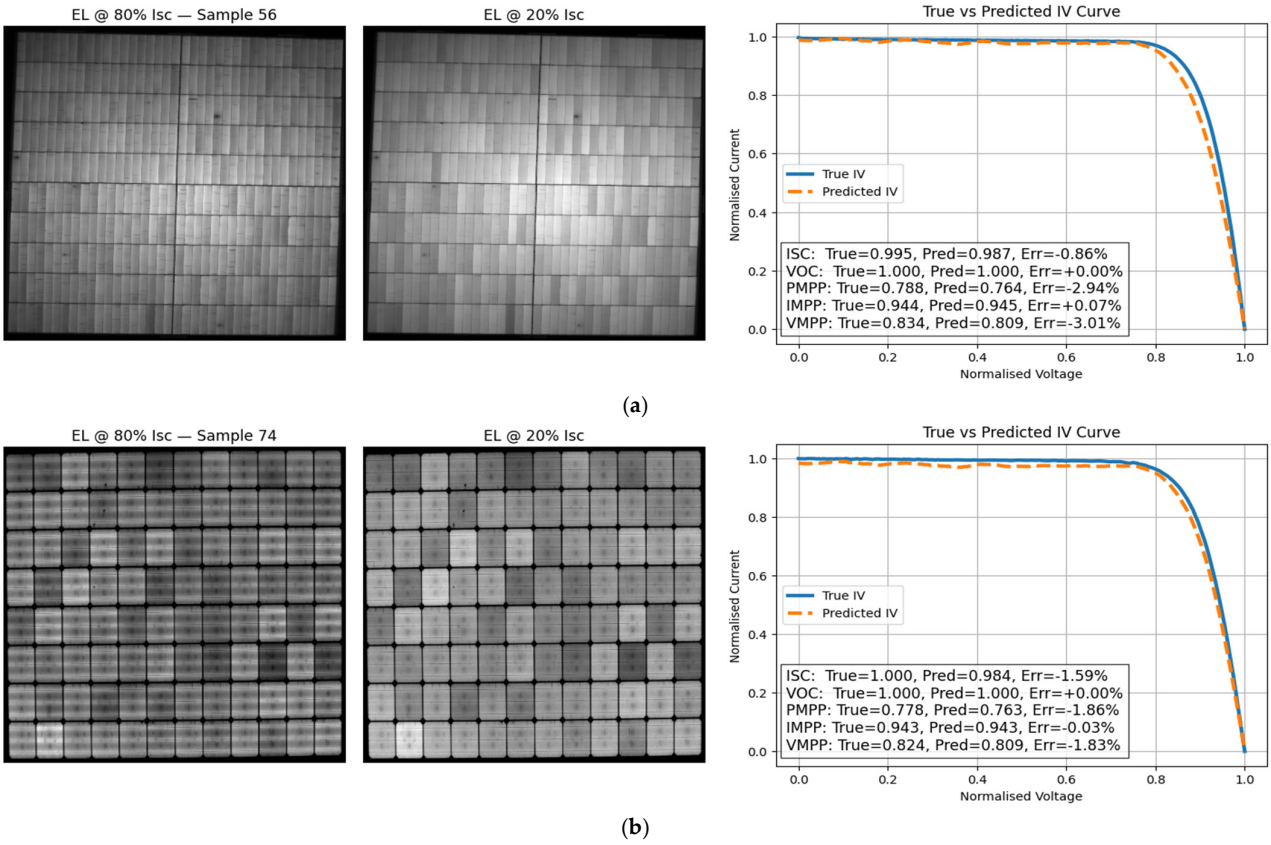

Figure 7. Output EL-to-IV model evaluation: (**a**) Corresponding EL images and IV comparison for Sample 56; (**b**) Corresponding EL images and IV comparison for Sample 74.

Figure 7a shows PV sample 56, which displays a comparatively uniform EL response in both EL80 and EL20 images, with only subtle luminance variations across the module. Such modules typically exhibit limited localized defect activity, and the corresponding electrical behavior is expected to be relatively smooth. Consistent with this, the predicted IV curve closely follows the measured curve over the full operating range. Errors across the five key electrical parameters remain below approximately 3.0%, with particularly strong agreement for Isc and Voc. The slight deviation in $Pmpp$ (≈3.0%) is attributable to the sensitivity of the maximum power point to small distortions near the knee of the IV curve, yet the model still reliably captures the curve's overall shape and slope.

PV sample 74 (see Figure 7b) represents a visually more heterogeneous module, characterized by numerous darker cells and a checkerboard-like EL pattern. Such luminance variations are typically associated with a combination of resistive losses and reduced minority carrier lifetimes. Despite this increased spatial complexity, the EL-to-IV model maintains high predictive accuracy, with errors in all electrical parameters remaining within ±1.9%. Notably, the predicted $Impp$ and Voc exhibit excellent alignment with the ground truth,

confirming that the model continues to extract meaningful electrical information even when supplied with substantially non-uniform emission patterns.

3.2. Statistical Evaluation Across the Full Test Set

To complement the qualitative case studies presented in Section 3.1, the proposed EL-to-IV prediction model was further evaluated across the entire population of 150 unseen PV modules. This comprehensive assessment provides a more robust indication of model generalization, as the test set encompasses a wide variety of luminance distributions, material characteristics, defect morphologies, and degradation severities. For each module, the EL-to-IV model was tasked with predicting the full IV curve as well as the associated electrical parameters (Isc, Voc, $Pmpp$, $Impp$, $Vmpp$) solely from the paired EL20 and EL80 images. The resulting prediction errors, computed relative to the corresponding measured IV curves, were aggregated to quantify overall accuracy and reliability.

Figure 8 presents the distribution of parameter-specific prediction errors across all test samples. The error distributions exhibit narrow interquartile ranges for all electrical parameters, with the mean error (indicated by the green markers) remaining within ±2% for $Pmpp$, $Impp$, and $Vmpp$, and within ±2.5% for Isc. Notably, the Voc predictions show virtually zero error across the entire dataset, demonstrating that the model reliably captures voltage-related behaviour even under substantial spatial variability in EL emission patterns since the EL emission is exponentially dependent on the PV module's voltage [15]. Although a small number of outliers appear in power-related parameters, primarily associated with modules exhibiting atypical degradation signatures, these remain limited in magnitude and do not affect overall performance trends.

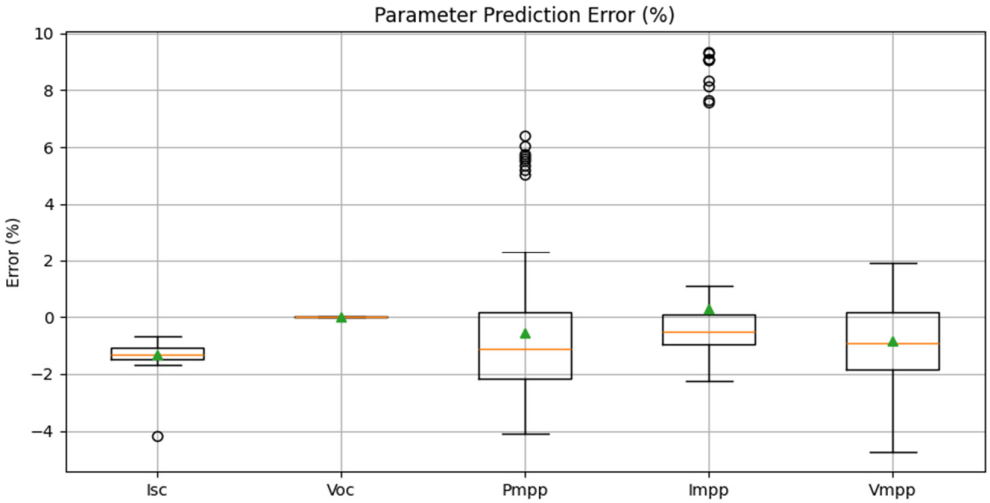

Figure 8. Distribution of prediction errors (%) for all 150 unseen PV modules across the five key electrical parameters. Boxplots show the interquartile range, with orange horizontal lines indicating the median, whiskers representing the full error spread, black circular markers denoting outliers, and green triangular markers indicating the mean error for each parameter.

The quantitative metrics in Table 4 further reinforce these observations. The mean absolute error (MAE) remains low across all parameters, with 1.315% for Isc, 1.921% for $Pmpp$, and effectively 0% for Voc. The corresponding root mean squared error (RMSE) values follow a similar pattern, confirming the model's stability and low variance in predictive performance. Importantly, the mean signed error indicates that predictions do not suffer from systematic bias; for instance, the negative mean error for Isc (−1.315%) suggests a slight underestimation tendency, whereas $Pmpp$ errors remain centred close to zero (−0.569%). Collectively, these results demonstrate that the model generalises

effectively beyond the training distribution, providing accurate IV reconstructions across a diverse set of real-world PV module conditions.

Table 4. Summary of statistical error metrics for the EL-to-IV model evaluated on the full test dataset of 150 unseen PV modules.

Parameter	MAE (%)	RMSE (%)	Mean Error (%)
Isc	1.315	1.369	−1.315
Voc	0.000	0.000	0.000
Pmpp	1.921	2.431	−0.569
Impp	1.458	2.726	0.293
Vmpp	1.357	1.672	−0.841

Although a small number of outliers appear in power-related parameters, including *Impp*, these correspond to modules with atypical degradation signatures or higher sensitivity of the maximum power point to small deviations in the knee region of the IV curve; consequently, while individual *Impp* errors may exceed 2% in isolated cases, the mean and median errors remain within the reported threshold, as reflected by the distribution statistics in Table 4.

3.3. Effect of Single-Condition EL Imaging on IV Prediction Performance

To further assess the robustness and practical deployability of the proposed EL-to-IV framework, the model was evaluated using only a single EL image per PV module, captured either at EL80 or EL20. Notably, the developed model can predict the IV curve independently of the current injection level at which the EL image is acquired. This experiment is particularly relevant for real-world field inspections, where EL measurements are typically taken at a single operating point, most commonly at high injection levels (80–100% *Isc*) due to the increased signal intensity, feature clarity and straightforward setup. Using the same test module, the model was run twice: once with only the EL80 image and once with only the EL20 image. The resulting predicted IV curves and key electrical parameters are presented in Figure 9.

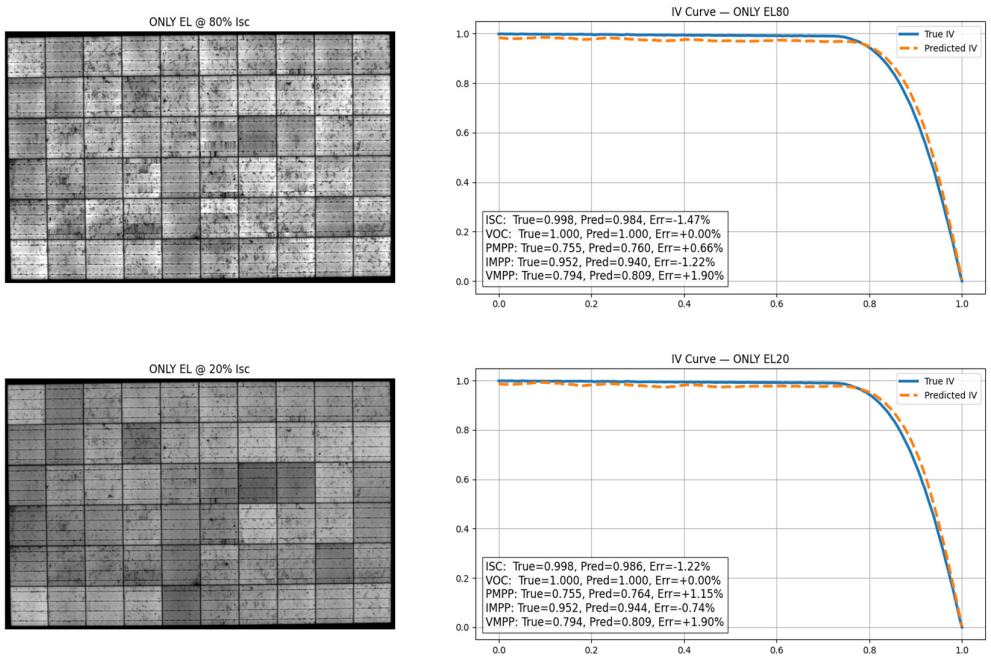

Figure 9. Example demonstration of IV curve prediction using a single EL image. Top row: prediction using only the EL80 image. Bottom row: prediction using only the EL20 image.

Although the proposed EL-to-I–V model is trained using a two-channel input tensor constructed from paired EL images acquired at 20% and 80% of *Isc*, single-image evaluation was performed by replicating the available EL image across both input channels. Specifically, when only one EL image was provided (either EL20 or EL80), the same image was duplicated to form a 512 × 512 × 2 input tensor. This strategy preserves the expected input dimensionality of the network while allowing the model to infer the IV curve from a single operating condition without architectural modification or retraining.

Remarkably, according to the results presented in Figure 9, the model retained near-identical prediction accuracy compared with the dual-input (EL80 + EL20) configuration. For both single-input cases, the predicted IV curve closely overlapped with the true measured IV curve, with errors in all the electrical parameters remaining within approximately 1–2% from the true measured values. These results indicate that the trained model has learned a highly generalizable mapping between EL spatial luminance patterns and the underlying electrical behavior of the PV module.

The only notable requirement emerging from these tests is the need for a high-quality EL image, irrespective of whether it is captured at EL80 or EL20. When the EL input signal is clean and well contrasted, the model successfully reconstructs the IV curve with very low errors. Interestingly, EL20 images exhibit a marginally better performance than EL80 in this study. This behavior is likely influenced by the defect severity present in the investigated modules, where moderate or early-stage defects may be sufficiently visible at lower injection levels. For modules exhibiting more severe degradation, larger cracks, or pronounced shunting effects, a stronger contrast difference between EL80 and EL20 is typically expected, which may alter the relative performance of the two operating points.

From a practical perspective, this remains a valuable outcome for field applications, as a single EL capture, most commonly at ≥80% Isc (or ideally at 100% Isc), is considerably easier and more practical to obtain. Consequently, the demonstrated single-image prediction capability enhances the model's operational practicality and significantly reduces the data collection burden in real PV inspection scenarios (e.g., drone-based EL inspections [16,28]).

3.4. Failure Case Analysis and Model Sensitivity to Image Pre-Processing

Although the EL-to-IV prediction model demonstrates consistently high accuracy across the full test set of 150 unseen PV modules, a small number of samples exhibited notable deviations between the predicted and measured IV curves. These failure cases offer valuable insights into the limitations of the approach and the conditions under which prediction reliability may degrade. Figure 10 presents two representative examples, illustrating how incorrect image pre-processing or artefacts in the EL input can adversely affect the reconstructed electrical characteristics. These two examples are representative instances of the outliers previously observed in Figure 8, where the model's performance deteriorates due to compromised EL image quality, leading to deviations in the predicted IV curves. Note that IV curves are normalized using the measured Isc; in these failure cases, small Isc measurement errors contribute to the apparent discrepancy between true and predicted curves.

In Figure 10a, the EL80 and EL20 images correspond to a module for which the automated cropping stage incorrectly segmented the panel boundary, causing several cell rows to be shifted or partially truncated. Because the model relies on spatial consistency across cell grids, such misalignment produces an incorrect mapping between luminance patterns and the module's electrical response. Consequently, the predicted IV curve exhibits an unrealistic two-step behavior, including an artificial "knee" at mid-voltage; an artefact does not present in the true IV curve. This demonstrates that the model is highly sensitive to structural distortions introduced during pre-processing and highlights the need for robust quality checks (e.g., grid consistency checks) prior to model inference.

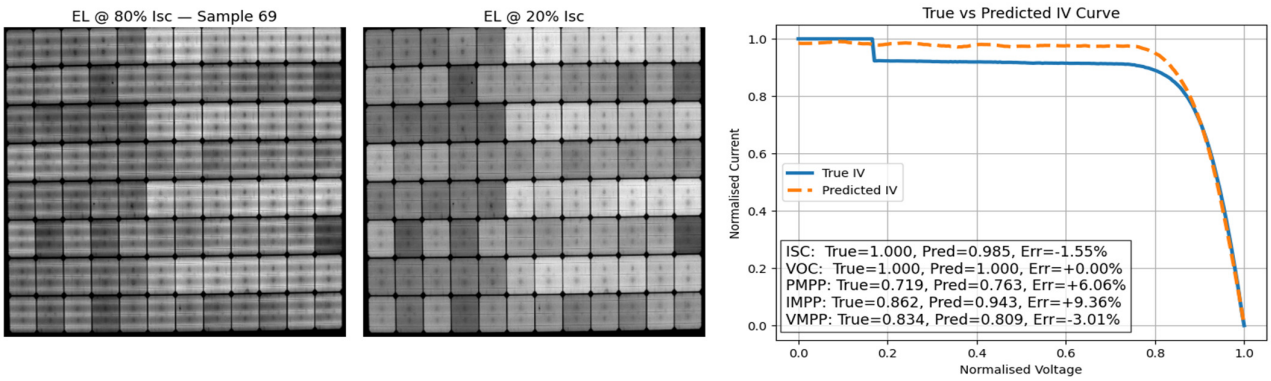

(**a**)

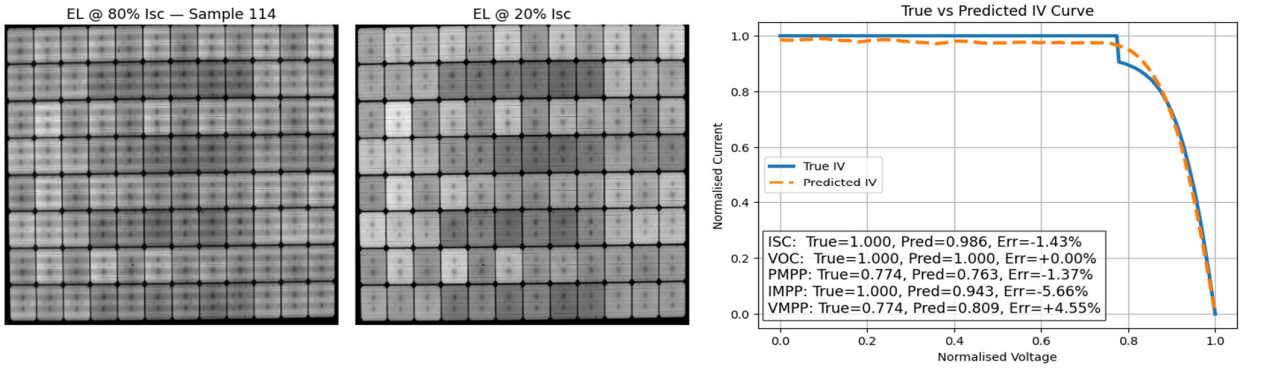

(**b**)

Figure 10. Failure cases of the EL-to-IV prediction model: (**a**) Corresponding EL images and I comparison for Sample 69; (**b**) Corresponding EL images and IV comparison for Sample 114.

A similar issue is visible in Figure 10b. Although the cropping is less severely misaligned, a cluster of cells appears substantially darker in the EL20 image due to overattenuated illumination or acquisition noise. The model, interpreting this dark patch as a severe localized degradation, overestimates the associated current loss. As a result, the predicted IV shows an exaggerated step-like drop before the MPP region, again deviating from the smooth true IV curve. Such examples show that the model can amplify local luminance artefacts, especially when the artefact mimics defect patterns seen during training.

3.5. Inference Speed and Practical Deployability

To assess the feasibility of deploying the proposed EL-to-IV framework in real inspection workflows, we evaluated the end-to-end inference time required to generate a complete IV curve from a pair of EL images (EL80 and EL20) across all 150 unseen test modules. Each sample was processed independently on the same hardware platform to ensure consistent timing measurements. The inference time reflects exclusively the forward pass of the trained model, not including file input/output (I/O) or preprocessing overheads, thereby representing a realistic estimate of model execution latency during field or laboratory deployment.

Figure 11 presents the inference time measured for each of the 150 modules. The results demonstrate that the model achieves consistently fast prediction speeds, with a median inference time of 397.74 ms, indicating that most modules can be processed in well under half a second. The mean inference time was 527.84 ms, slightly elevated due to a small number of outliers, including one instance where inference exceeded 5 s. These outliers are expected in Python-based deep-learning environments using CUDA-enabled GPUs on shared cloud infrastructure and are likely to arise from transient resource contention or GPU

initialization overhead, rather than from model complexity [29,30]. Aside from these rare cases, the overall distribution of execution times is tightly concentrated: the 95th percentile is 716.85 ms, and the minimum recorded inference time is 364.72 ms, confirming that the model is both computationally efficient and highly stable. Such performance indicates that the proposed framework is suitable for near-real-time PV module characterization, even when processing large batches of EL images or operating on portable GPU/edge devices in future deployments.

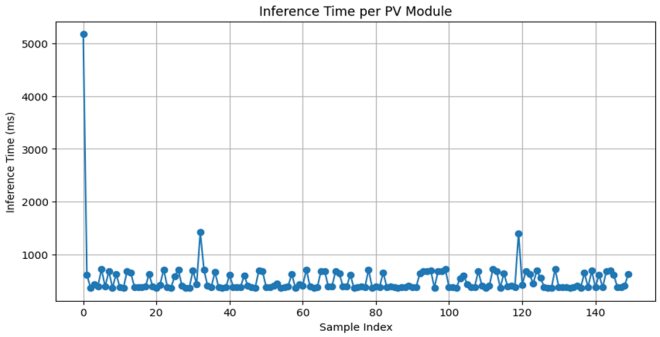

Figure 11. EL-to-IV model inference time (in milliseconds) required to generate an IV curve from paired EL80 and EL20 images across all 150 test PV modules.

4. Discussion and Comparative Analysis

The results presented in Section 3 demonstrate that EL imaging can be transformed from a primarily qualitative diagnostic tool into a quantitative surrogate for electrical characterization. By directly reconstructing the full IV curve from EL images, the proposed framework enables non-contact, image-only assessment of photovoltaic module performance, which is particularly relevant for large-scale inspection campaigns, inaccessible installations, and drone-based EL surveys. The ability to achieve sub-second inference further supports near-real-time deployment in both laboratory and field environments.

Despite these advantages, several limitations must be acknowledged. The model is sensitive to EL image quality and pre-processing accuracy, particularly with respect to cropping, alignment, and luminance artefacts, as demonstrated in the failure-case analysis. In addition, the model is trained on crystalline silicon modules represented in the public Sandia dataset and may not generalize directly to other technologies or module architectures without retraining. Furthermore, although normalization preserves the relative shape of the IV curve, absolute electrical ratings are not recovered, and the predictions should be interpreted as normalized electrical behavior rather than direct replacements for certified IV measurements.

A direct comparison can be made between the proposed CNN-based EL-to-IV framework and the recent transformer-based approach reported by [31], which represents the only available study that predicts full IV curves from EL images using the same publicly available dataset. While both approaches share the objective of reconstructing the complete IV curve from EL imagery, they differ substantially in model architecture, data representation, and practical deployment considerations. The authors in [31] employ a Swin Transformer architecture trained to predict a 400-point normalized IV curve from a single EL image, primarily acquired at high current injection levels. Their results demonstrate excellent accuracy for key electrical parameters such as *Isc*, *Voc*, and *Pmpp*, with mean errors below 1%, but also highlight challenges in accurately predicting parameters derived from sensitive regions of the curve, such as shunt resistance and dark current. The authors further note limitations in generalization when applying the trained model to EL images collected under different experimental conditions.

In contrast, our work adopts a compact CNN architecture that maps paired EL images acquired at complementary bias levels to a 200-point IV representation. Rather than focusing on transformer-based global attention, the proposed model emphasizes localized spatial feature extraction combined with explicit smoothness regularization to preserve physically meaningful IV behavior. Although the output discretization is coarser than in [31], the achieved accuracy for current- and power-related parameters remains within 1–2% on unseen test modules, while inference times are consistently below 0.5 s per module, supporting real-time scalability.

Importantly, the present study further demonstrates that reliable IV reconstruction can be achieved using a single EL image at either low or high injection levels, whereas [31] primarily relies on a single high bias EL condition. This flexibility reduces acquisition constraints and enhances suitability for field deployment. Taken together, the comparison indicates that while transformer-based approaches offer strong representational capacity, compact CNN-based models can achieve comparable electrical prediction accuracy with reduced computational complexity and greater operational flexibility.

5. Conclusions

This paper introduced EL-to-IV, a deep learning framework that directly predicts complete photovoltaic IV curves from EL images, addressing a key limitation of current EL-based diagnostics, which typically provide defect labels or indirect performance indicators rather than full electrical characterization. Using a publicly available dataset containing paired EL images at two injection levels (EL20 and EL80) and corresponding measured IV curves, the proposed convolutional neural network was trained to perform high-dimensional regression to a 200-point, normalized IV representation.

Across an unseen test set of 150 PV modules, the model reconstructed IV curves with high fidelity, producing low errors in key electrical parameters (e.g., MAE values on the order of ~1–2% for current- and power-related metrics, and negligible error for voltage-related behavior as reported). In addition to strong statistical performance, representative case studies demonstrated close agreement between predicted and measured IV curves over the full operating range. Importantly, inference speed was consistently fast, with a median runtime of ~0.4 s per module, supporting near-real-time deployment in inspection workflows.

A practical contribution of this work is the demonstration that single condition EL imaging (EL20 or EL80 alone) can still yield comparable IV prediction accuracy when image quality is high, reducing acquisition burden for field inspections. However, failure-case analysis revealed that the method is sensitive to EL image quality and pre-processing, particularly mis-cropping, misalignment, and luminance artefacts that can introduce non-physical steps in the predicted IV curve. These observations motivate future work on automated EL quality control, robust segmentation/cropping pipelines, and confidence-aware prediction.

Future research should also evaluate generalization under broader operational variability (e.g., different module technologies, measurement protocols, and outdoor/daylight EL regimes) and incorporate uncertainty quantification and physics-consistent constraints (e.g., monotonicity and smoothness enforcement) to further improve reliability. Overall, EL-to-IV advances EL imaging from qualitative defect visualization towards quantitative, image-only electrical characterization, enabling scalable PV performance assessment without direct electrical tracing.

Author Contributions: Conceptualization, M.D. and R.G.V.; methodology, M.D., G.A.d.R.B. and P.B.P.; software, M.D.; validation, G.A.d.R.B. and R.G.V.; resources, P.B.P.; data curation, M.D., R.G.V. and G.A.d.R.B.; writing—original draft preparation, M.D.; writing—review and editing, G.A.d.R.B., R.G.V. and P.B.P. All authors have read and agreed to the published version of the manuscript.

Funding: This research received no external funding.

Data Availability Statement: The EL images and corresponding IV curves used to train and validate the proposed CNN model are sourced from a publicly available dataset https://data.openei.org/submissions/8378 accessed on 28 January 2026.

Conflicts of Interest: The authors declare no conflicts of interest.

Appendix A

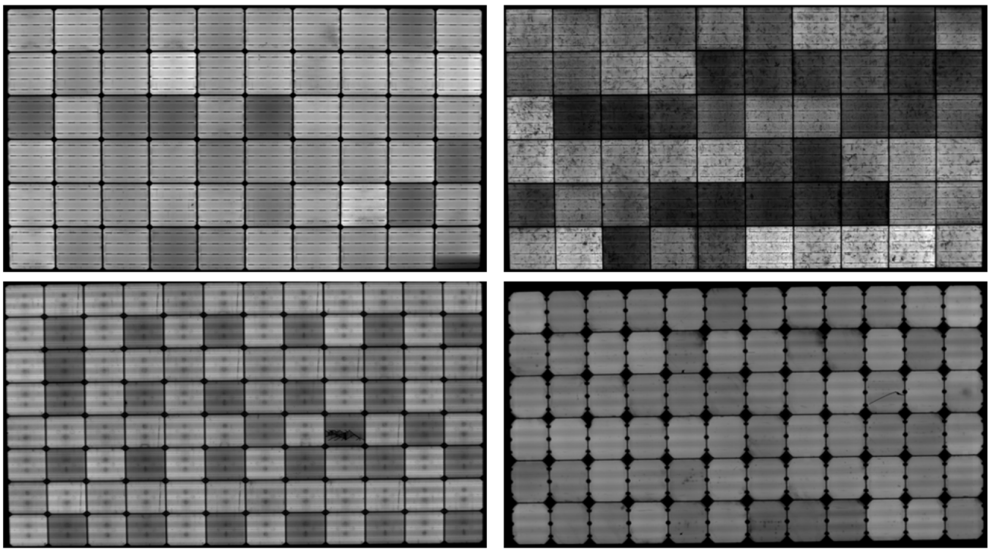

Figure A1. Representative examples of EL images from four different PV modules included in the dataset. The images illustrate variations in spatial luminance patterns and defect characteristics across modules, highlighting differences in cell-level behavior and overall module condition.

References

1. Kumar, V.; Maheshwari, P. Advanced analytics on I–V curves and electroluminescence images of photovoltaic modules using machine learning algorithms. *Prog. Photovolt. Res. Appl.* **2022**, *30*, 880–888. [CrossRef]
2. Li, B.; Hansen, C.W.; Chen, X.; Diallo, D.; Migan-Dubois, A.; Delpha, C.; Jain, A. A robust I–V curve correction procedure for degraded photovoltaic modules. *Renew. Energy* **2024**, *224*, 120108. [CrossRef]
3. Olayiwola, T.N.; Hyun, S.H.; Choi, S.J. Photovoltaic modeling: A comprehensive analysis of the I–V characteristic curve. *Sustainability* **2024**, *16*, 432. [CrossRef]
4. Dhimish, M.; d'Alessandro, V.; Vieira, R.; Mellit, A.; Spataru, S.V.; Benatto, G.A.D.R. Evaluation of the multi-year-on-year method for degradation analysis in photovoltaic systems. *Renew. Energy* **2025**, *255*, 123772. [CrossRef]
5. Rahman, T.; Mansur, A.A.; Hossain Lipu, M.S.; Rahman, M.S.; Ashique, R.H.; Houran, M.A.; Elavarasan, R.M.; Hossain, E. Investigation of degradation of solar photovoltaics: A review of aging factors, impacts, and future directions toward sustainable energy management. *Energies* **2023**, *16*, 3706. [CrossRef]
6. Hijjawi, U.; Lakshminarayana, S.; Xu, T.; Fierro, G.P.M.; Rahman, M. A review of automated solar photovoltaic defect detection systems: Approaches, challenges, and future orientations. *Sol. Energy* **2023**, *266*, 112186. [CrossRef]
7. Liu, Y.; Ding, K.; Zhang, J.; Li, Y.; Yang, Z.; Zheng, W.; Chen, X. Fault diagnosis approach for photovoltaic array based on the stacked auto-encoder and clustering with I–V curves. *Energy Convers. Manag.* **2021**, *245*, 114603. [CrossRef]
8. Dhanraj, J.A.; Mostafaeipour, A.; Velmurugan, K.; Techato, K.; Chaurasiya, P.K.; Solomon, J.M.; Gopalan, A.; Phoungthong, K. An effective evaluation on fault detection in solar panels. *Energies* **2021**, *14*, 7770. [CrossRef]
9. Zhang, Z.; Ma, M.; Ma, W.; Zhang, R.; Wang, J. A data-driven photovoltaic string current mismatch fault diagnosis method based on I–V curve. *Microelectron. Reliab.* **2022**, *138*, 114705. [CrossRef]

10. De Riso, M.; Hassan, S.; Guerriero, P.; Dhimish, M.; Daliento, S. Enhanced photovoltaic panel diagnostics: Advancing a high-precision and low-cost I–V curve tracer. *IEEE Trans. Instrum. Meas.* **2024**, *73*, 9006110. [CrossRef]
11. Koester, L.K.; Vallarella, E.; Louwen, A.; Lindig, S.; Moser, D. Evaluating the effects of photovoltaic module heating during electroluminescence inspection. *EPJ Photovolt.* **2023**, *14*. [CrossRef]
12. Carpintero, L.A.; Terrados, C.; González-Francés, D.; Sulca, K.P.; Alonso, V.; González, M.A.; Martínez, O. Electroluminescence inspections of PV modules and strings by a self-powering configuration in daylight mode. *Sol. Energy* **2025**, *301*, 113913. [CrossRef]
13. Jaeckel, B.; Pander, M.; Schenk, P.; Linsenmeyer, A.; Kirch, J. Nomenclature and description of electro-luminescence (EL) observations: Cell cracks and other observations. *EPJ Photovolt.* **2024**, *15*, 44. [CrossRef]
14. Dhimish, M.; Ahmad, A.; Tyrrell, A.M. Inequalities in photovoltaic modules reliability: From packaging to PV installation site. *Renew. Energy* **2022**, *192*, 805–814. [CrossRef]
15. Fuyuki, T.; Kondo, H.; Kaji, Y.; Ogane, A.; Takahashi, Y. Analytic findings in the electroluminescence characterization of crystalline silicon solar cells. *J. Appl. Phys.* **2007**, *101*, 023711. [CrossRef]
16. Mahdavipour, Z. Defect inspection of photovoltaic solar modules using aerial electroluminescence (EL): A review. *Sol. Energy Mater. Sol. Cells* **2024**, *278*, 113210. [CrossRef]
17. Liu, Q.; Liu, M.; Wang, C.; Wu, Q.J. An efficient CNN-based detector for photovoltaic module cells defect detection in electroluminescence images. *Sol. Energy* **2024**, *267*, 112245. [CrossRef]
18. Drir, N.; Mellit, A.; Blasuttigh, N.; Pavan, A.M. Enhancing defect detection in photovoltaic cells through advanced cascade CNN with attention mechanisms on electroluminescence images. *Energy Convers. Manag.* **2026**, *348*, 120636. [CrossRef]
19. Hassan, S.; Dhimish, M. Broad-scale electroluminescence analysis of 5 million+ photovoltaic cells for defect detection and degradation assessment. *Renew. Energy* **2024**, *237*, 121868. [CrossRef]
20. Drir, N.; Chekired, F.; Mellit, A.; Blasuttigh, N. Hybrid CNN–EML model for fault diagnosis in electroluminescence images of photovoltaic cells. *Renew. Energy* **2025**, *250*, 123343. [CrossRef]
21. Drir, N.; Mellit, A.; Bettayeb, M.; Dhimish, M. Enhanced photovoltaic defect detection using perceptual loss in DCGAN and VGG16-integrated models on electroluminescence images. *IEEE J. Photovolt.* **2025**, *15*, 759–769. [CrossRef]
22. Abro, G.E.M.; Ali, A.; Memon, S.A.; Memon, T.D.; Khan, F. Strategies and challenges for unmanned aerial vehicle-based continuous inspection and predictive maintenance of solar modules. *IEEE Access* **2024**, *12*, 176615–176629. [CrossRef]
23. Buerhop, C.; Bommes, L.; Schlipf, J.; Pickel, T.; Fladung, A.; Peters, I.M. Infrared imaging of photovoltaic modules: A review of the state of the art and future challenges facing gigawatt photovoltaic power stations. *Prog. Energy* **2022**, *4*, 042010. [CrossRef]
24. del Prado Santamaría, R.; Dhimish, M.; dos Reis Benatto, G.A.; Kari, T.; Poulsen, P.B.; Spataru, S.V. From indoor to daylight electroluminescence imaging for PV module diagnostics: A comprehensive review of techniques, challenges, and AI-driven advancements. *Micromachines* **2025**, *16*, 437. [CrossRef] [PubMed]
25. Bosman, L.B.; Leon-Salas, W.D.; Hutzel, W.; Soto, E.A. PV system predictive maintenance: Challenges, current approaches, and opportunities. *Energies* **2020**, *13*, 1398. [CrossRef]
26. Zheng, Q.; Tan, D.; Wang, F. Improved convolutional neural network based on fast exponentially linear unit activation function. *IEEE Access* **2019**, *7*, 151359–151367. [CrossRef]
27. Macêdo, D.; Zanchettin, C.; Oliveira, A.L.; Ludermir, T. Enhancing batch normalized convolutional networks using displaced rectifier linear units: A systematic comparative study. *Expert Syst. Appl.* **2019**, *124*, 271–281. [CrossRef]
28. Tang, W.; Yang, Q.; Hu, X.; Yan, W. Edge intelligence for smart EL image defect detection of PV plants in IoT-based inspection systems. *IEEE Internet Things J.* **2022**, *10*, 3047–3056. [CrossRef]
29. Wang, Z.; Jiang, Z.; Wang, Z.; Tang, X.; Liu, C.; Yin, S.; Hu, Y. Enabling latency-aware data initialization for integrated CPU/GPU heterogeneous platform. *IEEE Trans. Comput.-Aided Des. Integr. Circuits Syst.* **2020**, *39*, 3433–3444. [CrossRef]
30. Pang, W.; Luo, X.; Chen, K.; Ji, D.; Qiao, L.; Yi, W. Efficient CUDA stream management for multi-DNN real-time inference on embedded GPUs. *J. Syst. Archit.* **2023**, *139*, 102888. [CrossRef]
31. Byford, B.K.; Boucheron, L.E.; King, B.H.; Braid, J.L. Advanced Photovoltaic Module Characterization: Using Image Transformers for Current–Voltage Curve Prediction from Electroluminescence Images. *IEEE J. Photovolt.* **2025**, *15*, 557–565. [CrossRef]